Moment Tensor Estimation of Event S1222a and Implications for Tectonics Near the Dichotomy Boundary in Southern Elysium Planitia, Mars

R. Maguire[1*], V. Lekic[2], D. Kim[3], N. Schmerr[2], J. Li[4], C. Beghein[4], Q. Huang[5], J. C. E. Irving[6], F. Karakostas[2,7], P. Lognonné[8], S. C. Stähler [3], W. B. Banerdt[9]

[1]Department of Earth Science and Environmental Change, University of Illinois Urbana-Champaign, Champaign, IL, USA.

[2]Department of Geology, University of Maryland, College Park, MD,USA.

[3]Institute of Geophysics, ETH Zürich, Zürich, Switzerland.

[4]Department of Earth, Planetary, and Space Sciences, University of California, Los Angeles, Los Angeles, CA, USA.

[5]Department of Geophysics, Colorado School of Mines, Golden, CO, USA.

[6]School of Earth Sciences, University of Bristol, Bristol, UK.

[7]Istituto Nazionale di Geofisica e Vulcanologia, Bologna, Italy

[8]Institut de Physique du Globe de Paris, Université de Paris, CNRS, Paris, France.

[9]Jet Propulsion Laboratory, California Institute of Technology, Pasadena, CA, USA.

Corresponding author: Ross Maguire (rossrm@illinois.edu)

Key Points:

- We performed a moment tensor inversion of S1222a based on waveform fitting of both body and surface waves.
- The scalar moment of S1222a is between 3.5×10^{15} – 5.0×10^{15} Nm.
- S1222a likely resulted from dip slip faulting in the crust on an E-W to SE-NW striking fault plane.

Abstract

On May 4th, 2022 the InSight seismometer SEIS recorded the largest marsquake ever observed, S1222a, with an initial magnitude estimate of Mw 4.7. Understanding the depth and source properties of this event has important implications for the nature of tectonic activity on Mars. Located ~37 degrees to the southeast of InSight, S1222a is one of the few non-impact marsquakes that exhibits prominent ratio surface waves. We use waveform modeling of body waves (P and S) and surface waves (Rayleigh and Love) to constrain the moment tensor and quantify the associated uncertainty. We find that S1222a likely resulted from dip-slip faulting in the mid-crust (source depth ~18 – 28 km) and estimate a scalar moment of 3.5×10^{15} – 5.0×10^{15} Nm (magnitude Mw 4.3 – 4.4). The best-fitting focal mechanism is sensitive to the choice of phase windows and misfit weights, as well as the structural model of Mars used to calculate Green's functions. We find that an E-W to SE-NW striking thrust fault can explain the data well, although depending on the choice of misfit weighting, a normal fault solution is also permissible. The orientation of the best-fitting fault plane solutions suggests that S1222a takes place on a fault system near the martian crustal dichotomy accommodating relative motion between the northern lowlands and southern highlands. Independent constraints on the event depth and improved models of the (an)isotropic velocity structure of the martian crust and mantle could help resolve the ambiguity inherent to single-station moment tensor inversions of S1222a and other marsquakes.

Plain Language Summary

The InSight lander's sensitive seismometer recorded over 1,000 marsquakes during the course of its mission. Like the Earth, it is thought that the majority of quakes on Mars result from faulting events that release stress within the planetary interior. Understanding the nature of these events, including their magnitude, depth, and faulting style provides valuable clues into planetary deformation and its driving forces. In this study, we use seismic waveform modeling to constrain the properties of the S1222a event, the largest marsquake recorded during the InSight mission. We find that S1222a likely resulted from faulting within the crust of Mars, and estimate the event was equivalent to a 4.3 – 4.4 magnitude event on Earth. Our analysis places constraints on the geometry of the fault plane, although it is difficult to conclusively determine if S1222a resulted from compressional or extensional forces. The ambiguity arises from the sensitivity of the analysis to subjective parameter choices. Further advances may be possible if more accurate models of the interior structure of Mars become available.

1 Introduction

Seismic moment tensors provide key insights into the orientation of active faults, slip across faults, and the distribution of stress in planetary interiors. On Earth, moment tensors are routinely calculated following significant seismic events (e.g. Dziewonski and Woodhouse, 1983) and have played a crucial role in understanding global patterns of seismicity as well as deformation across tectonic settings (e.g., Ekström et al., 2012). Techniques to constrain source characteristics of teleseismic events typically rely on data from globally distributed seismic stations, and optimal focal mechanisms are found either by fitting body wave first motions (e.g. Brumbaugh, 1979) or by fitting waveforms of intermediate period body wave (Langston and Helmberger, 1975) or surface wave phases (e.g. Arvidsson and Ekstrom, 1998), or complete long period waveforms (e.g. Dziewonski et al. 1981). Information about source depth comes from the

lag-time of depth phases (e.g. Basham and Ellis, 1969) and/or by the frequency dependence of surface wave excitation (e.g. Tsai and Aki, 1970).

On Mars, moment tensor inversions are challenging for three reasons: 1) only a single seismic station is available, limiting the sampling of the focal sphere; 2) depth phases are only rarely unequivocally identified rendering source depth estimates inaccurate; and, 3) contribution of along-path structure to waveforms is difficult to estimate due to unknown three-dimensional (3D) structure. However, since different seismic phases have different radiation patterns and sample different portions of the focal sphere, single station moment tensor inversions are possible for sufficiently high-quality events, provided that sufficiently accurate structural models are available.

After more than two martian years on the surface, the InSight (Interior Exploration using Seismic Investigations, Geodesy, and Heat Transport, Banerdt et al. 2020) lander and associated seismometer (Lognonné et al., 2019) has helped transform our understanding of the interior and dynamics of Mars. InSight landed in the Elysium Planitia of Mars on November 16, 2018 and has recorded over 1,000 marsquakes (Ceylan et al., 2022) with distinct spectral characteristics (e.g. Giardini et al. 2020), revealing seismo-tectonically active zones (e.g., Stähler et al., 2022). The majority of the observed marsquakes are low-magnitude high frequency (HF) events with energy above 2.4 Hz, which have been interpreted as having crustal propagation paths and have helped determine the physical properties of the shallow subsurface (Lognonné et al., 2020; Karakostas et al., 2021; Menina et al., 2021). Although larger low-frequency (LF) and broadband (BB) marsquakes with mantle traversing paths are less commonly observed, these events have been key for constraining the deep interior structure of Mars, including crustal structure below (Knapmeyer-Endrun et al., 2021; Kim et al., 2021a; Li et al., 2022a; Durán et al., 2022a) and away (Kim et al. 2022a, 2022b; Li et al. 2022c, 2022d) from InSight, crustal anisotropy (Beghein et al. 2022; Kim et al. 2022b; Li et al. 2022b), upper mantle seismic wave speed (Khan et al., 2021; Durán 2022b), the radius of the core (Stähler et al., 2021; Khan et al., 2022, Durán et al., 2022a), and mineral phase transitions in the deep mantle (Huang et al., 2022).

Prior to the arrival of InSight on Mars, reverse faulting due to planetary contraction driven by secular cooling was expected to be one of the principal drivers of seismicity (Solomon et al., 1991). Thus far, however, seismic evidence of ongoing tectonic activity has come from the Cerberus Fossae extensional graben system which has been a prominent source of both HF and LF marsquakes (Stähler et al., 2022). Moment tensor estimates based on detailed waveform fitting of body waves from Cerberus Fossae events S0173a and S0235b implied extension along steeply dipping normal faults with roughly E-W strike orientations (Brinkman et al., 2021). Alternatively, based on body wave polarities and relative amplitudes, Sita & van der Lee (2022) found that S0173a can be best fit as a marsquake doublet that starts as a thrust followed by oblique normal faulting. They also found that S0235b likely represents vertical dip-slip motion with a small normal faulting component. Recently, Jacob et al., (2022) estimated moment tensor solutions from nine high-quality LF and broadband (BB) marsquakes located in Cerberus Fossae and surrounding regions using P and S waveform fits, secondary phase amplitudes, and a lack of surface wave detection criteria. They found that two of the events (S0325a and S0784a) located south of Cerberus Fossae near the martian crustal dichotomy boundary are consistent with thrust

faulting source mechanisms. Additionally, they located the hypocenters of all nine tectonic events to moderate depths in the crust (15 – 36 km).

On May 4th, 2022, InSight recorded the seismic event S1222a, the largest marsquake observed during the mission, with an initial estimated moment magnitude of Mw 4.7 (Kawamura et al., 2022). Despite occurring in the early afternoon during a period of high background noise due to strong winds, InSight's very broad band seismometer, SEIS VBB (Lognonné et al., 2019), recorded some of the clearest seismic waveforms of any marsquake observed during the InSight mission (Fig 1). S1222a was designated a quality A event by the Mars Quake Service (MQS) due to its high signal-to-noise ratio and the identification of both body and surface wave phases with clear polarization (Kawamura et al., 2022). Waveform data from SEIS is archived and made publicly available by the InSight Mars SEIS Data Service (InSight Mars SEIS Data Service, 2019). Several prominent instrument glitches are present during the event (Fig. 1D). Although glitches have been shown to be capable of influencing seismic analysis and interpretation (Kim et al., 2021b), no glitches are apparent near the phases of interest in this study. Importantly, both Love and Rayleigh waves were identified in the waveforms of S1222a with no glitches (Kawamura et al., 2022); modeling of fundamental-mode dispersion (Beghein et al., 2022) together with overtones (Kim et al., 2022b) revealed substantial large-scale radial anisotropy in the martian crust. The observation of Rayleigh and Love waves also provides complementary constraints on the moment tensor, which have not been available to other marsquake moment tensor inversions.

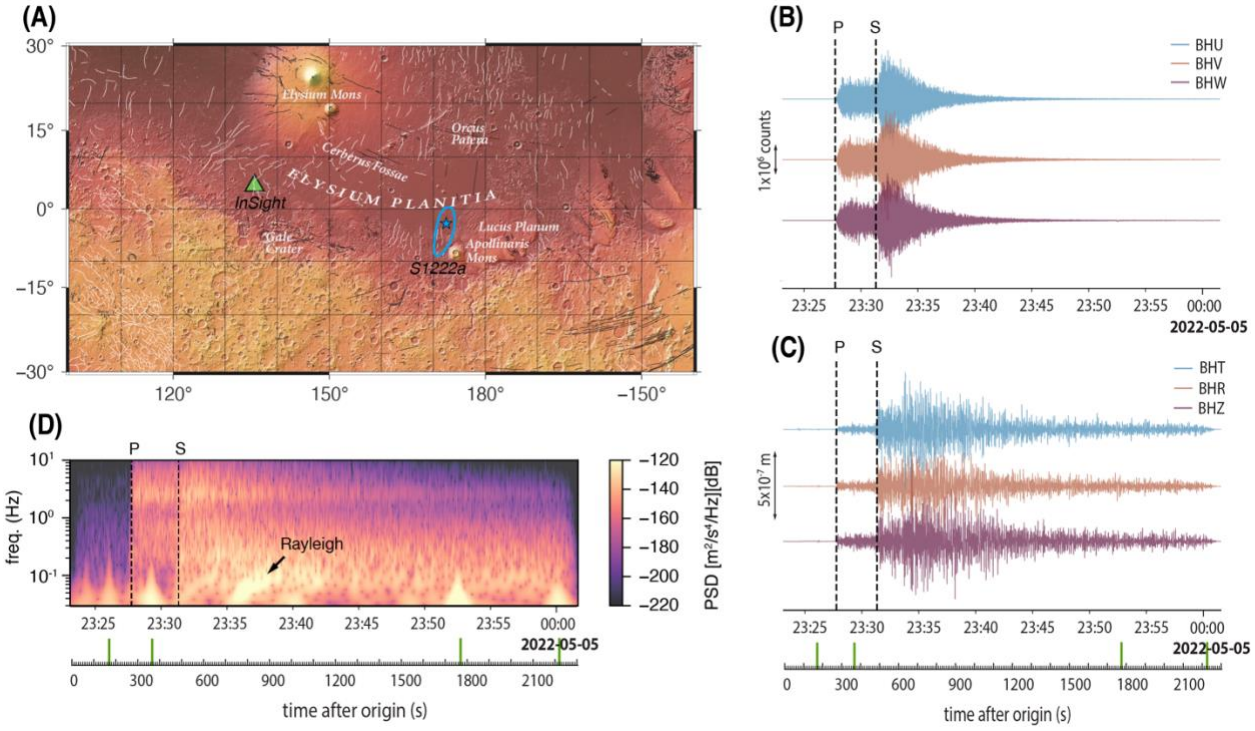

Figure 1. (A) Map showing the location of InSight (green triangle) and the MQS reported location of S1222a (blue star, with uncertainty ellipse) (Kawamura et al., 2022). Thin white and black lines indicate mapped compressional and extensional faults, respectively, from the database of Knapmeyer et al. (2006). (B) Raw recordings of S1222a from the SEIS VBB instrument. The dashed vertical lines show the MQS arrival times of P and S. (C) Same as (B) but the data is instrument corrected and rotated to vertical

(BHZ), radial (BHR), and transverse (BHT) components using a back azimuth of 107.7 degrees. All components are bandpass filtered between 0.1 - 0.6 Hz. (D) Spectrogram of BHZ data. Vertical green lines on the lower time axis mark clearly apparent instrument glitches.

In this paper, we use seismic waveforms from both body waves (P and S) and, for the first time, surface waves (Rayleigh and Love) to estimate the best-fitting magnitude, depth, and focal mechanism of S1222a. We take advantage of available models of the crustal structure along the S1222a minor-arc paths, which were obtained by modeling the group velocity dispersion of Rayleigh and Love minor arc phases (Beghein et al., 2022) and their overtones (Kim et al. 2022b). We outline a strategy for marsquake moment tensor inversion based on a grid search approach which allows uncertainty estimation on event depth and faulting style.

2 Moment tensor inversion

For S1222a, the MQS reported an origin time of UTC 2022-05-04T23:23:07 (+/- 4.8 s) and an epicentral distance of 37 +/- 1.6 degrees, based on the S – P differential travel times (InSight Marsquake Service, 2023). Additionally, based on the P-wave polarization, the back azimuth of the event was reported to be 101^o, although subsequent analysis by MQS based on body wave polarization attributes measured in multiple frequency bands suggested a bimodal distribution of likely back azimuths, with peaks between 96^o and 112^o. While the discrepancies between estimates of back azimuth (and therefore source location) are of geophysical interest and could potentially be informative of 3D propagation effects along the path, the exceptional signal-to-noise ratio and clear polarization of P strongly suggests a source location in southern Elysium Planitia, northwest of Apollinaris Mons (Fig 1A).

We estimate the best-fitting moment tensor solution of S1222a by inverting waveforms of P, S, Rayleigh, and Love wave phases recorded by SEIS VBB. Even though moment tensor estimation is a linear inverse problem for a fixed velocity model, the determination of source depth is not. Optimal phase alignment between synthetic and observed waveforms is achieved by alignment based on cross-correlation, as commonly done in regional moment tensor inversions on Earth (e.g. Dreger et al., 2021); this alignment introduces an additional nonlinearity into the moment tensor inversion. Therefore, we choose to use a grid search approach. The synthetic waveforms are computed using Instaseis (van Driel et al., 2015), which allows rapid retrieval of pre-computed Green's functions based on AxiSEM waveform simulations (Nissen-Meyer et al., 2014). The velocity model used to compute synthetic waveforms is a modified version of the KKS21_GP model (Stähler et al., 2021), in which the upper 80 km is replaced with a radially anisotropic model based on fitting both Rayleigh and Love wave dispersion measurements of S1222a (Beghein et al., 2022) (Fig. S1). The shear attenuation quality factor Q_μ is assumed to be 600 in the crust and mantle (e.g., Giardini et al., 2020).

The event location and origin time are essential parameters for performing a moment tensor inversion. Here, we fix the origin time to the time reported by MQS and locate the event using the reported back-azimuth. We assume an epicentral distance of 36.0^o based on the S – P travel time difference of our preferred velocity model. While uncertainties in the location of the event will introduce uncertainties in the estimations of source properties, we find that our analysis is insensitive to small shifts in source location within the uncertainty bounds of the reported distance and back azimuth of S1222a.

Prior to waveform fitting, raw data are instrument-corrected and rotated to the radial (R), transverse (T), and vertical (Z) components. Body wave data are filtered between 3 – 12 s and surface wave data are filtered between 14 – 36 s using a fourth-order nonzero-phase Butterworth filter. The number of cycles for these waves during their propagation from origin is therefore relatively low and about 40, 70 and 30 for P, S, and surface waves (see Table 1), justifying an elastic model with low attenuation. Scattering effects could however still reduce the amplitudes. For each seismic phase, we manually select the windows in which to fit seismic waveforms. For the P-wave, we fit both the Z and R component waveforms in a window starting 10 s before and ending 25 s after the first arriving P energy. For S-waves, we fit waveforms on the T and R components and use a window starting 10 s before and 15 s after the onset of S. The arrival of S on the Z component is unclear, so we omit it from the inversion. Minor arc Rayleigh waveforms are fitted on both Z and R and the Love waveform is fitted on T. Both Rayleigh and Love waves are fitted in 300 s long windows.

To account for small travel time shifts between observed and predicted data, synthetic waveforms are aligned by cross-correlation prior to calculating the misfit. The maximum allowed travel time shifts are +/- 5 s for P waves, +/- 10 s for S waves and +/- 60 s for Rayleigh and Love waves. To account for uncertainties in the anisotropic velocity model a relative shift between Rayleigh and Love waves of up to +/- 5 s is allowed. This translates to a velocity uncertainty of ~0.02 km/s, which is smaller than the measurement error assumed in the structural inversions of Kim et al., (2022b) and Beghein et al., (2022).

The best-fitting double-couple solution for each possible depth is found by searching over a grid spanning the range of possible values of strike, dip, and rake, with 60 grid points in each dimension. M_W is varied between 4.2 and 5.0 in increments of 0.05. This search is performed for source depths between 0 – 100 km, with a depth increment of 2 km.
For every step in the grid search the misfit χ is calculated using Equation 1 following alignment of observed and synthetic waveforms that maximizes their cross-correlation:

$$\chi = \sum_{i=1}^{N} w_i \int_0^T \left\| d_i^{obs} - d_i^{syn} \right\|^2 \mathrm{d}t \qquad \text{(Equation 1)}$$

where d_i^{obs} and d_i^{syn} are the observed and synthetic displacement waveforms in the *i*th window, respectively, *N* is the number of windows, *T* is the window length, and w_i is a weighting factor. Although the choice of phase windows and weights is subjective, it is an important parameter in waveform-based moment tensor inversions. Here, we use two different approaches for weighing body wave and surface wave windows. In the first approach, we apply weights to body waves and surface waves that are inversely proportional to the L2 norm of the observed data vector to ensure that each phase contributes equally to the total misfit. The windows and weights used for the inversion are shown in Table 1. In the second approach, we use the same weights as before, but we amplify the weight in the first 15 s of the P-wave window five times compared to the rest of the window to emphasize the importance of fitting the initial polarity of the P-wave, which may have a smaller amplitude than later arriving phases.

Phase	Window start (UTC)	Window end	Window weight	Components	Diff Time (sec) and Q cycle
P	2022-05-04T23:27:34	2022-05-04T23:28:09	45	Z,R	285/38
S	2022-05-04T23:31:15	2022-05-04T23:31:40	8	R,T	501/67
R1	2022-05-04T23:33:57	2022-05-04T23:38:57	1	Z,R	800/32
L1	2022-05-04T23:32:17	2022-05-04T23:37:17	4	T	700/28

Table 1. Windows and weights used for inversion. Diff start time is the differential time between middle of the window and quake origin time. Number of Q cycles are computed with central periods of 7.5 and 25 for body and surface waves.

3 Results

3.1 Even weighting

Figure 2 shows the results of the double couple grid search over source depths of 0 – 100 km, for inversions using even weights for body and surface wave phases. Inversions were performed using both body waves and surface waves together (Fig. 2A), body waves only (Fig. 2B), and surface waves only (Fig. 2C). From here on, we refer to inversions of both body waves and surface waves as BW+SW inversions, and inversions of only body waves or only surface waves as BW or SW inversions, respectively. The lowest misfits of BW+SW inversions are found for sources in the depth range of ~18 – 28 km. In this depth range, the predominant focal mechanism of the best fitting BW+SW solutions is a thrust with a roughly E-W striking fault plane. Thrust fault solutions are mostly found in this depth range for BW and SW inversions, but for BW inversions, a SE-NW striking fault plane is preferred. BW inversions favor events in a similar depth range, although the misfit surface varies more strongly with depth, due to the influence of depth phases. For SW inversions, the misfit varies more smoothly with depth, with the best-fitting solutions found for a source near 26 km. A second minimum in the misfit function near 4 km depth suggests that a shallow source cannot be ruled out from SW inversions alone. Events deeper than ~50 km are considered unlikely because the misfit generally increases with increasing depth beyond this range for all inversion types. Below, we outline two plausible scenarios for focal mechanisms at different depths in the crust based on the total misfit and detailed assessment of important aspects of the waveform fits such as body wave first motions.

The first scenario we consider is a source at 8 km depth (green beachball in Fig. 2A), which is shown in Fig 3A. Although a source depth at 8 km is not in the region of lowest misfit, we include it because its misfit is lower than most other shallow sources, particularly for BW inversions. The best-fitting focal mechanism for the BW+SW grid search is a Mw 4.35 (scalar moment, $M_0 = 4.2\times10^{15}$ Nm), predominantly reverse fault, with nodal planes striking either E-W or SE-NW. The P-wave is fitted as the large pulse with an onset near 18 s in the P-wave window. Although the synthetics provide a good match for both the amplitude and wave shape of this signal, the first arriving energy at the P-wave onset time identified by MQS (black arrows, Fig. 2) is not fitted. This is because the signal near the MQS-identified P-wave onset has a small amplitude, and thus will have a minor influence on the overall misfit in the P-wave window. Predicted S-waveforms align well with the observed signal with an onset near 10 s in the S-wave window, although amplitudes are slightly underestimated. The predicted Rayleigh wave signal for this moment tensor provides an excellent fit to the observed amplitudes, although the amplitude in the early portion of the signal is underestimated. Synthetic Love waves are in good

agreement with both amplitude and phase of the observations. The absolute travel time shift Δt of the Rayleigh wave is 12.0 s and the relative shift between Rayleigh and Love waves Δt_R is 2.15 s. Focal mechanisms need not require small absolute travel time shifts of body or surface wave phases because they could reflect uncertainties in source location or errors in the velocity model between their different paths through the interior. However, because our crustal velocity model already includes radial anisotropy that explains well the observed group velocities of minor arc Love and Rayleigh waves, focal mechanisms that imply small relative shifts between Rayleigh and Loves should be preferred.

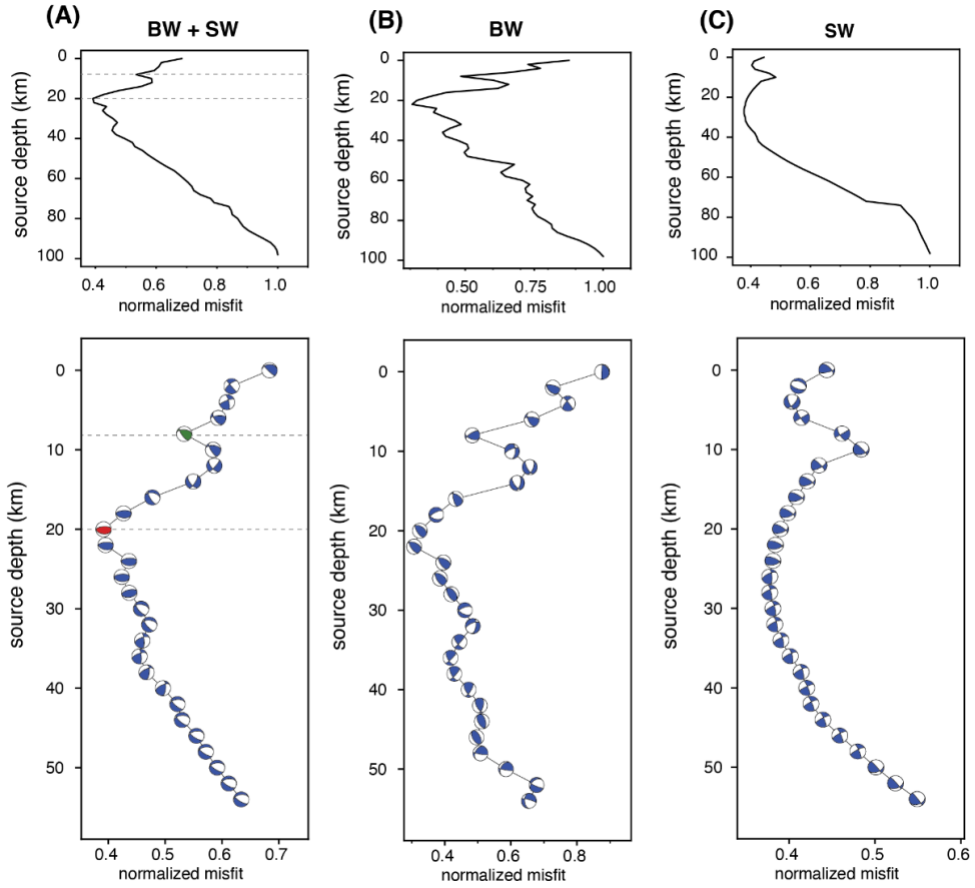

Figure 2. Inversion misfit for a range of source depths. Panels (A), (B), and (C), show results for BW+SW, BW, and SW inversions, respectively. In each panel, the top figure shows the normalized misfit for the full grid search depth range, and the bottom panel shows the best-fitting moment tensor solutions for source depths shallower than 55 km. The green and red focal mechanisms in (A) represent the two scenarios shown in Figure 3.

Figure 3B shows the second scenario we consider, which is for a source at 20 km depth (red beachball in Fig. 2). The magnitude of the best-fitting solution Mw 4.4 and the source represents thrusting along an E-W oriented fault plane. The P-wave fit in this scenario is similar to the source at 8 km depth, although the first arriving P-wave energy is a small downward pulse that strongly resembles the observed signal near the MQS identified P-wave time, but with a later onset. This suggests a possible explanation for the P-waveform, in which the small initial pulse identified as the P-wave arrival by MQS (black arrows in Fig. 3) is the direct P which is near

nodal takeoff, and the subsequent energy arriving ~8 s later is the depth phase pP (Fig. S2). If this is the case, the timing between P and pP provides a strong constraint on the source depth. An alternative explanation is that the first two arrivals represent two discrete events (e.g., Sita et al., 2022), with a small foreshock occurring ~8 seconds before a larger event. The S-waveform fits also show good agreement with observed amplitudes and satisfy the first motions, and the predicted surface wave fits are similar to the previous case, although the Rayleigh wave phase prediction more clearly matches the observations. Interestingly, if we place this thrust fault solution at the surface, the peak waveform amplitudes of most phases are well fitted, although the small initial P-wave pulse is not reproduced (Fig. S3). Therefore, body waves of S1222a do not seem compatible with a surface source.

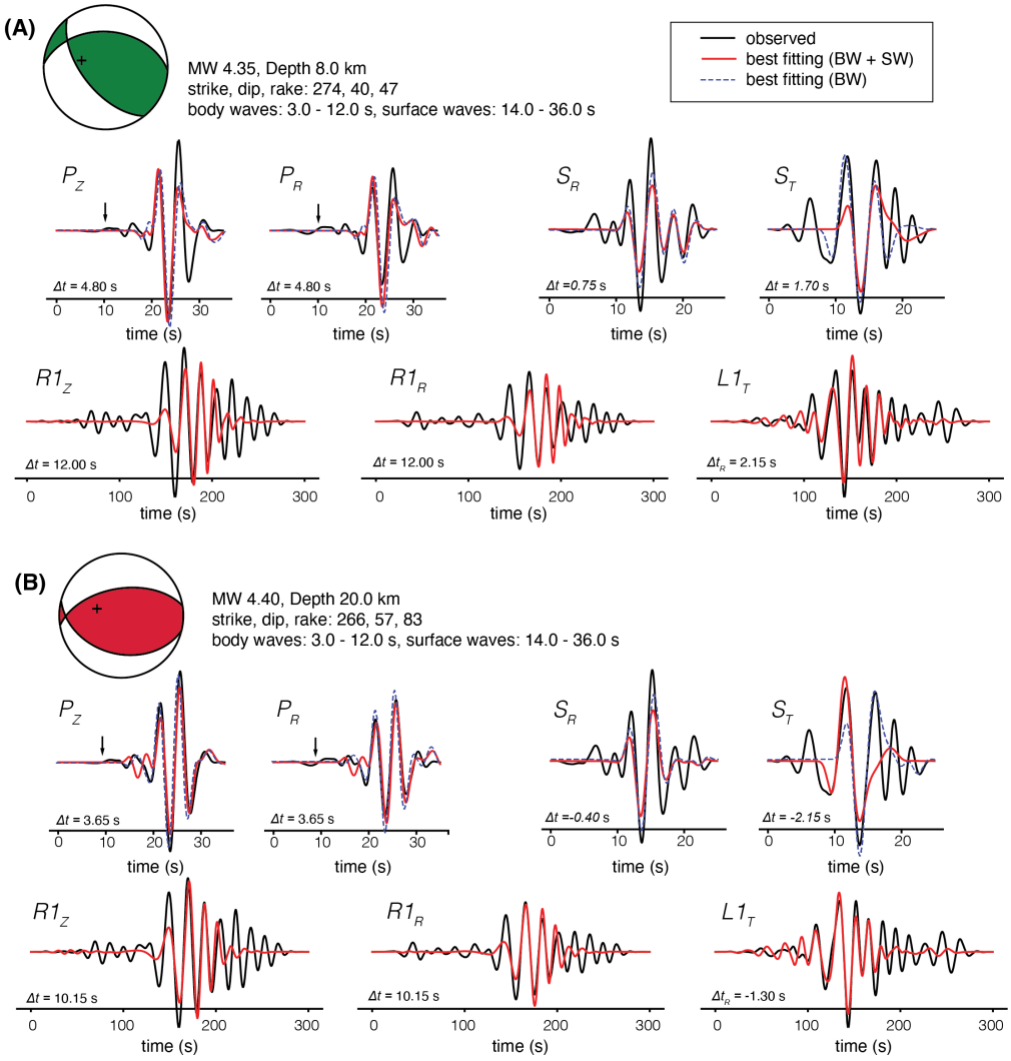

Figure 3. Best-fitting moment tensors and the corresponding waveform fits shown for source depths at 8 km (A), and 22 km (B). Observed waveforms are shown in black and synthetic waveforms of BW+SW and BW inversions are shown in red lines and blue dashed lines respectively. Beachball solutions shown in the top left of each panel represent the best-fitting moment tensor for BW+SW inversions. The + symbol represents the piercing point of the P-wave on the focal-sphere. The black arrows indicate the MQS reported P-wave arrival. The label to the upper left of each waveform indicates the phase (P,S,R1,L1) and component of ground motion (Z,R,T).

An additional trend observed is that estimated moment magnitudes are generally lower than the initial MQS estimate of Mw = 4.7, which is based on analysis of the amplitude spectrum. Here, we find moment tensor magnitudes for plausible scenarios range between approximately Mw = 4.3 – 4.4 (M_0 = 3.5x10^{15} – 5.0×10^{15} Nm). Additionally, we find a correlation between event depth and estimated magnitude. For example, the mean and standard deviation of the magnitudes of the best fitting moment tensors is Mw = 4.42 +/- 0.16 (M_0 between 3.1x10^{15} – 9.3×10^{15} Nm) for source depths between 0 – 50 km, and Mw = 4.71 +/- 0.08 (M_0 between 1.1x10^{16} – 1.92×10^{16} Nm) for source depths between 50 – 100 km. Thus, a deeper source implies a larger magnitude, although deeper events are less likely due to their larger misfit values.

3.2 Heavily weighted P-wave first arrival

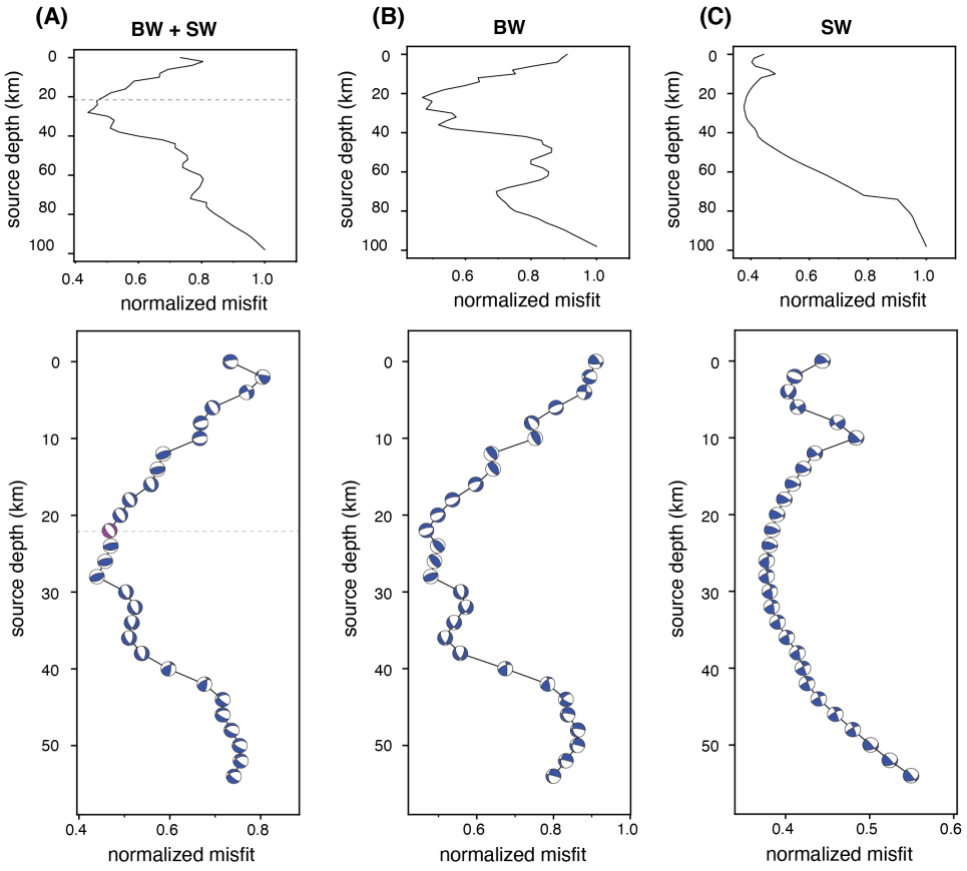

Figure 4. Same as Fig. 2, but for inversions with a higher weight applied to the early part of the P-wave window

The potential importance of inversions that emphasize fitting the relatively low amplitude, early part of the P-wave is illustrated in Figure 4. When the first 15 s of the P-wave window are up-weighted by a factor of 5, the best-fitting solutions of BW+SW inversions are found in a similar depth range as previous inversions, but the focal mechanism solutions are different (Fig. 4A). For sources near 20 km depth, where evenly weighted inversions found E-W striking thrust fault solutions, a SE-NW striking normal fault provides the best solution. The waveform fits for the

best-fitting normal fault solution at 22 km depth (purple beachball in Fig. 4A), are shown in Fig. 5A. In this case, both the low amplitude signal near the MQS P-wave pick and the larger subsequent arrivals are well fitted (correlation coefficient 0.91). Overall, surface wave fits are similar to those shown in Fig 3B (thrust fault solution at 20 km depth), although the early arriving long period Rayleigh wave signal appears to be reproduced better. The lowest misfit value is found for a source at 28 km depth, where the best-fitting solution is an ENE-WSW striking thrust fault (Fig. S4).

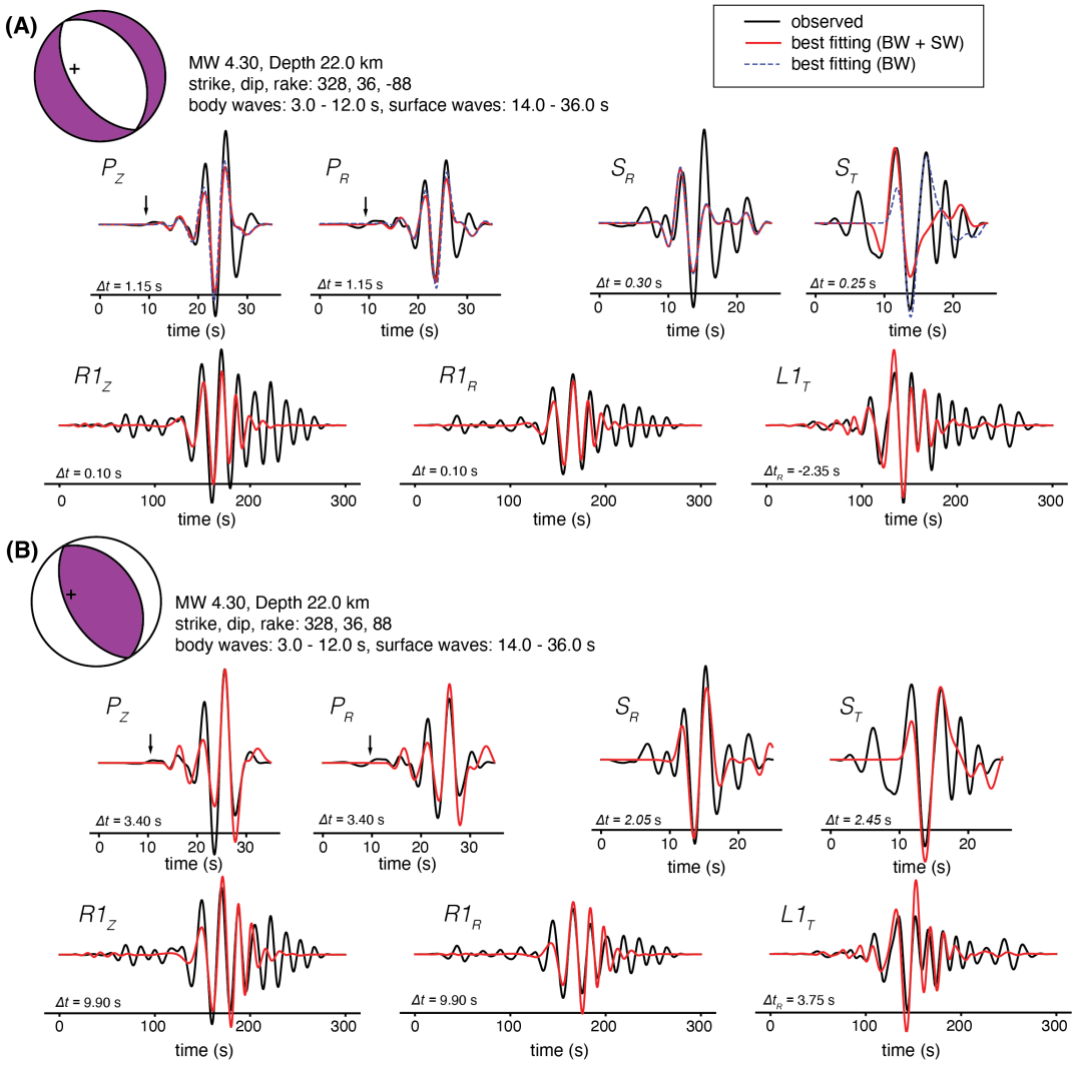

Figure 5. (A) Same as Fig. 3, but a high weight was applied to the early portion of the P-wave window. The best-fitting moment tensor and waveform fits are shown for a source at 22 km depth (purple beachball shown in Fig. 4A). (B) Predicted waveforms for a reverse fault with the same strike and dip as the focal mechanism shown in panel (A).

Understanding the uncertainties of moment tensor inversions is important for making robust inferences about crustal faulting mechanisms. Here, we take a grid search approach that allows assessment of the misfit over the full range of possible double couple moment tensors. Figure 6 shows cross sections through the 3D misfit volume for a source at 22 km depth, for an inversion emphasizing the early part of the P-wave window. The structure of the misfit volumes is

complex with multiple local minima, some of which may not be significantly larger in value than the global minimum. For example, although the global minimum of the inversion for a source at 22 km depth suggests a normal fault solution (black circles in Fig 6), the misfit slice in Fig 6C is almost symmetrical, indicating that a thrust fault solution on a similarly oriented fault plane can achieve a similar data fit. Fig. 5B shows waveform fits for a thrust fault solution assuming a source at 22 km depth and the same fault plane orientation as the best-fitting normal fault solution.

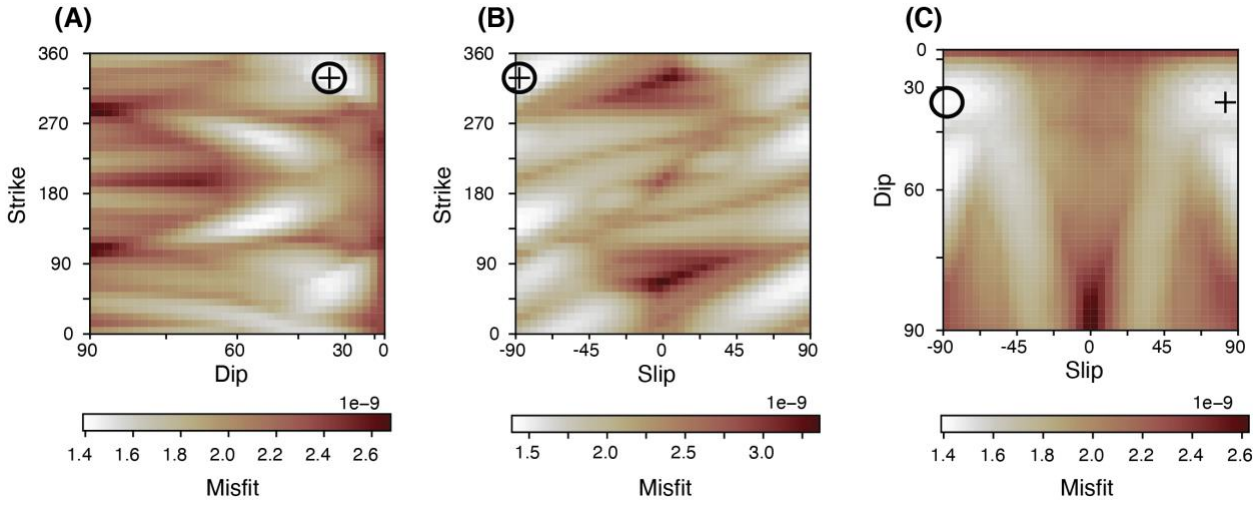

Figure 6. Cross sections through the 3D misfit volume of a grid search using a source depth of 22 km. The early portion of the P-wave window was more heavily weighted in the misfit function. The black circles show the location of the best-fitting moment tensor solution (Fig. 5A), and the + symbol shows the location of the reverse fault solution shown in Fig. 5B.

4 Discussion

Without definitive detection of body wave depth phases the source depth of S1222a is uncertain. Giardini et al., (2020) proposed that LF events likely originate in the uppermost mantle, which could explain the lack of high frequencies that would be attenuated away in the mantle. Since then, other observed marsquakes have challenged this paradigm. For example, high frequency energy (> 5 Hz) has been observed from teleseismically detected impacts (Posiolova et al., 2022; Kim et al., 2022a) with mantle traversing body waves.

The signal duration may provide an additional depth discriminant because shallow events are likely to produce longer coda due to extensive scattering in the near-surface (e.g., van Driel et al., 2021; Karakostas 2022). S1222a has one of the longest durations of any recorded marsquake, above 8 hours for the multiple orbit surface waves and about an hour in the body wave coda (see Fig. 1), which suggests a shallow origin. Without more precise knowledge of the subsurface structure along the path, this remains fairly qualitative speculation. For Cerberus Fossae events, the corner frequency may be indicative of source depth because the lower corner frequencies of LF events compared to HF events are thought to result from their origin in deeper, warmer, structurally weaker zones (Stähler et al., 2022). Similarly, shallow moonquakes exhibit higher corner frequencies than deep moonquakes, likely indicating a high-stress drop (Oberst, 1987). Outside of Cerberus Fossae, LF events generally have higher corner frequencies, making the relationship between source depth and corner frequency less clear. The high corner frequency

observed for S1222a (~ 4 Hz, see Kawamura et al. 2022) could result from a combination of high stress drop and a cold, weakly attenuating lithosphere.

The structural model used to generate Green's functions is a key component of moment tensor inversions. Ideally, 3D models that account for structural variations near the source and receiver would be used so that reflected and converted body wave phases can be accurately modeled. However, in this study we are limited to one-dimensional (1D) structural models owing to the lack of accurate knowledge of along-path variations in structure that are necessary to accurately simulate high frequency waveforms. Indeed, moment tensor inversions on Earth are often limited to lower frequencies when 1D structural models are used to compute Green's functions (e.g. Dreger and Helmberger, 1993). The structural model used here is based on fitting fundamental mode dispersion of Rayleigh and Love waves (Beghein et al., 2022), although our results do not change significantly if we use the model of Kim et al., (2022b), which fits both fundamental mode and overtone data (Fig. S5). Although using models constructed from surface wave dispersion enables accurate fitting of Rayleigh and Love waveforms, the model does not incorporate constraints on crustal layering below InSight. A structural model based on joint inversion of surface wave dispersion and receiver functions could potentially improve moment tensor estimations because waveform predictions would include converted and reflected body wave phases from discontinuities below InSight. Near-source scattering, however, would remain unaccounted for.

The likely source region of S1222a, to the northwest of Apollinaris Mons, lies near the martian hemispheric dichotomy boundary which divides the highly cratered southern highlands and less cratered northern lowlands. In this region, Knapmeyer et al., (2006) inferred the presence of relatively young (< 500 Ma) compressional faults based on wrinkle ridge structures that are likely to be the surface expression of blind thrusts at depth. The orientation of these faults is predominantly N-S, which is inconsistent with the best-fitting thrust fault solutions at most crustal depths, although this orientation cannot be ruled out (e.g., Fig 6). If S1222a indeed resulted from compressional faulting on one of these blind thrusts it would represent the first observation of a tectonically active wrinkle ridge system, and only the second confirmed seismically active tectonic feature on Mars beside the Cerberus Fossae system.

The majority of reverse faulting solutions represent crustal shortening along E-W or NE-SW oriented fault planes, which is roughly parallel to the outline of the dichotomy boundary. Jacob et al. (2022) inferred a similar focal mechanism for the marsquake S0784a, which likely occurred to the southeast of InSight near the dichotomy boundary. They suggest that S0784a resulted from motion along a fault that originally accommodated subsidence of the northern lowlands but has since been reactivated in a compressional regime due to planetary contraction. Although events S0784a and S1222a have different source locations, it is plausible that they represent the same tectonic environment.

Over the course of the InSight mission, the majority of significant marsquakes have been related to extensional tectonics in the Cerberus Fossae system, and compressional faulting due to planetary contraction did not appear associated with the observed seismic activity. Stähler et al., (2022) estimate that the Cerberus Fossae events account for an annual seismic moment release of $1.4\text{-}5.6\times10^{15}$ Nm/yr, or over half of seismic moment release in the InSight hemisphere. The

estimated scalar moment of S1222a is 3.5×10^{15} – 5.0×10^{15} Nm, suggesting that this event alone accounts for a large fraction of the annual seismic budget of Mars. If S1222a did result from compressional faulting, it may suggest that planetary thermal contraction is an ongoing source of seismicity on Mars, as was expected prior to the arrival of InSight, although it is questionable whether planetary cooling could generate such a large event. Thus, resolving the ambiguity in the focal mechanism of S1222a remains an important goal for understanding the nature of active tectonic deformation on Mars.

5 Conclusions

Based on waveform fits from P, S, Rayleigh, and Love wave phases, we estimated the source properties and focal mechanism of S1222a, the largest marsquake recorded during the InSight mission. Our approach, which included minimizing the L2 misfit between broadband observations and synthetic seismograms via a grid search allowed us to estimate the best-fitting magnitude and focal mechanism, as well as understand the uncertainties on the source parameters. We find that S1222a resulted from either reverse faulting or normal faulting along an E-W to SE-NW oriented fault plane at moderate depth in the crust (< 50 km). Potential depth phases suggest a source depth near 20 km, but the complexity of the signal does not rule out a shallower source at 5-10 km depth. The estimated moment magnitude of S1222a is Mw = 4.3 – 4.4 (M_0 between 3.5×10^{15} – 5.0×10^{15} Nm), lower than initially determined by MQS. The most likely fault plane orientation is roughly parallel to the dichotomy boundary, potentially indicating either extension along boundary faults accommodating subsidence of the northern lowlands, or reactivation of fault systems in a compressional regime (e.g., Jacob et al., 2022). We cannot rule out the possibility that S1222a occurred on a blind thrust fault associated with wrinkle ridge deformation. Future work may be able to provide tighter constraints on the focal mechanism of S1222a (and other marsquakes) if improved structural models of Mars become available, or if additional seismic phases are clearly identified.

Acknowledgments

Our moment tensor inversion was based on a modified version of the MTUQ code package (https://github.com/uafgeotools/mtuq), and we thank the developers for making this tool openly available. Seismic data from the S1222a event, and other marsquakes, is available for download through the IRIS Data Management Center. This paper is InSight contribution number 290. The authors acknowledge the NASA, the CNES, their partner agencies and Institutions (UKSA, SSO, DLR, JPL, IPGP-CNRS, ETHZ, IC, and MPS-MPG) and the flight operations team at JPL, SISMOC, MSDS, IRIS-DMC, and PDS for providing the SEED SEIS data. D.K. acknowledge support from the ETH+ funding scheme (ETH+02 19-1: “Planet Mars”). N.S. and V.L. were supported by NASA Grant 80NSSC18K1628. C.B. and J.L. were funded by NASA InSight PSP grant #80NS-SC18K1679. P.L acknowledges support from CNES and ANR (ANR-19-CE31-0008-08 MAGIS, ANR-18-IDEX-0001).

Open Research

Seismic data from the InSight mission is openly available from IRIS Data Management Center (https://ds.iris.edu/ds/nodes/dmc/), the InSight SEIS Data Service at IPGP (https://www.seis-

insight.eu/en/science/seis-data/seis-data-description), and the NASA Planetary Data System (https://pds-geosciences.wustl.edu/missions/insight/).

References

Arvidsson, R., & Ekström, G. (1998). Global CMT analysis of moderate earthquakes, Mw≧ 4.5, using intermediate-period surface waves. *Bulletin of the Seismological Society of America*, 88(4), 1003-1013.

Banerdt, W. B., Smrekar, S. E., Banfield, D., Giardini, D., Golombek, M., Johnson, C. L., ... & Wieczorek, M. (2020). Initial results from the InSight mission on Mars. *Nature Geoscience*, 13(3), 183-189.

Basham, P. W., & Ellis, R. M. (1969). The composition of P codas using magnetic tape seismograms. *Bulletin of the Seismological Society of America*, 59(2), 473-486.

Beghein, C., Li, J., Weidner, E., Maguire, R., Wookey, J., Lekić, V., ... & Banerdt, W.B. (2022). Crustal Anisotropy in the Martian lowlands from surface waves. *Geophysical Research Letters*, 49(24), e2022GL101508.

Böse, M., Stähler, S.C., Deichmann, N., … & Banerdt, W.B., (2021). Magnitude Scales for Marsquakes Calibrated from InSight Data. *Bulletin of the Seismological Society of America*. https://doi.org/10.1785/0120210045

Brinkman, N., Stähler, S. C., Giardini, D., Schmelzbach, C., Khan, A., Jacob, A., ... & Banerdt, W. B. (2021). First focal mechanisms of marsquakes. *Journal of Geophysical Research: Planets*, 126(4), e2020JE006546.

Brumbaugh, D. S. (1979). Classical focal mechanism techniques for body waves. *Geophysical Surveys*, 3(4), 297-329.

Ceylan, S., Clinton, J. F., Giardini, D., Stähler, S. C., Horleston, A., Kawamura, T., ... & Banerdt, W. B. (2022). The marsquake catalogue from InSight, sols 0–1011. *Physics of the Earth and Planetary Interiors*, 333, 106943.

Dreger, D. S., & Helmberger, D. V. (1993). Determination of source parameters at regional distances with three-component sparse network data. *Journal of Geophysical Research: Solid Earth*, 98(B5), 8107-8125.

Dreger, D. S., Gritto, R., & Nelson, O. (2021). Path calibration of the democratic People's Republic of Korea 3 September 2017 nuclear test. *Seismological Society of America*, 92(6), 3375-3385.

Durán, C., Khan, A., Ceylan, S., Zenhäusern, G., Staehler, S., Clinton, J. F., & Giardini, D. (2022a). Seismology on Mars: An analysis of direct, reflected, and converted seismic body waves with implications for interior structure. *Physics of the Earth and Planetary Interiors*, 325, 106851.

Durán, C., Khan, A., Ceylan, S., Charalambous, C., Kim, D., Drilleau, M., ... & Giardini, D. (2022b). Observation of a Core-Diffracted P-Wave From a Farside Impact With Implications for the Lower-Mantle Structure of Mars. *Geophysical Research Letters*, 49(21), e2022GL100887.

Dziewonski, A. M., Chou, T. A., & Woodhouse, J. H. (1981). Determination of earthquake source parameters from waveform data for studies of global and regional seismicity. Journal of *Geophysical Research: Solid Earth*, 86(B4), 2825-2852.

Dziewonski, A. M., & Woodhouse, J. H. (1983). An experiment in systematic study of global seismicity: Centroid-moment tensor solutions for 201 moderate and large earthquakes of 1981. *Journal of Geophysical Research: Solid Earth*, 88(B4), 3247-3271.

Ekström, G., Nettles, M., & Dziewoński, A. M. (2012). The global CMT project 2004–2010: Centroid-moment tensors for 13,017 earthquakes. *Physics of the Earth and Planetary Interiors*, 200, 1-9.

Giardini, D., Lognonné, P., Banerdt, W. B., Pike, W. T., Christensen, U., Ceylan, S., ... & Yana, C. (2020). The seismicity of Mars. *Nature Geoscience*, 13(3), 205-212.

Huang, Q., Schmerr, N. C., King, S. D., Kim, D., Rivoldini, A., Plesa, A. C., ... & Banerdt, W. B. (2022). Seismic detection of a deep mantle discontinuity within Mars by InSight. *Proceedings of the National Academy of Sciences*, 119(42), e2204474119.

InSight Marsquake Service (2023). Mars Seismic Catalogue, InSight Mission; V13 2023-01-01. ETHZ, IPGP, JPL, ICL, Univ. Bristol. https://doi.org/10.12686/a19

InSight Mars SEIS Data Service. (2019). Seis raw data, insight mission. IPGP, JPL, CNES, ETHZ, ICL, MPS, ISAE-Supaero, LPG, MFSC. Retrieved from https:// datacenter.ipgp.fr/networks/detail/XB_2016/ doi: 10.18715/SEIS.INSIGHT .XB_2016

Jacob, A., Plasman, M., Perrin, C., Fuji, N., Lognonné, P., Xu, Z., ... & Banerdt, W. B. (2022). Seismic sources of InSight marsquakes and seismotectonic context of Elysium Planitia, Mars. *Tectonophysics*, 229434.

Karakostas, F., Schmerr, N., Maguire, R., Huang, Q., Kim, D., Lekic, V., ... & Banerdt, B. (2021). Scattering Attenuation of the Martian Interior through Coda-Wave Analysis. *Bulletin of the Seismological Society of America*, 111(6), 3035-3054.

Kawamura, T., Clinton, J. F., Zenhäusern, G., Ceylan, S., Horleston, A. C., Dahmen, N. L., ... & Banerdt, W. B. (2022). S1222a-the largest Marsquake detected by InSight. *Geophysical Research Letters*, e2022GL101543.

Khan, A., Ceylan, S., van Driel, M., Giardini, D., Lognonné, P., Samuel, H., ... & Banerdt, W. B. (2021). Upper mantle structure of Mars from InSight seismic data. *Science*, 373(6553), 434-438.

Khan, A., Sossi, P. A., Liebske, C., Rivoldini, A., & Giardini, D. (2022). Geophysical and cosmochemical evidence for a volatile-rich Mars. *Earth and Planetary Science Letters*, 578, 117330.

Kim, D., Lekić, V., Irving, J. C.E., Schmerr, N., Knapmeyer-Endrun, B., Joshi, R., ... & Banerdt, W. B. (2021a). Improving constraints on planetary interiors with PPs receiver functions. *Journal of Geophysical Research: Planets*, 126(11), e2021JE006983.

Kim, D., Davis, P., Lekić, V., Maguire, R., Compaire, N., Schimmel, M., ... & Banerdt, W. B. (2021b). Potential pitfalls in the analysis and structural interpretation of seismic data from the Mars InSight mission. *Bulletin of the Seismological Society of America*, 111(6), 2982-3002.

Kim, D., Banerdt, W. B., Ceylan, S., Giardini, D., Lekić, V., Lognonné, P., ... & Panning, M. P. (2022a). Surface waves and crustal structure on Mars. *Science*, 378(6618), 417-421.

Kim, D., Stähler, S. C., Ceylan, S., Lekić, V., Maguire, R., Zenhäusern, G., ... & Banerdt, W. B. (2022b). Structure Along the Martian Dichotomy Constrained by Rayleigh and Love Waves and their Overtones. *Geophysical Research Letter*s, e2022GL101666.

Knapmeyer, M, Oberst, J., Hauber, E., Wählisch, M., Deuchler, C., and Wagner, R., Working Models for Spatial Distribution and Level of Mars' Seismicity (2006). *Journal of Geophysical Research E: Planet*s 111(11), 1–23. https://doi.org/10.1029/2006JE002708.

Knapmeyer-Endrun, B., Panning, M. P., Bissig, F., Joshi, R., Khan, A., Kim, D., ... & Banerdt, W. B. (2021). Thickness and structure of the martian crust from InSight seismic data. *Science*, 373(6553), 438-443.

Langston, C. A., & Helmberger, D. V. (1975). A procedure for modelling shallow dislocation sources. *Geophysical Journal International*, 42(1), 117-130.

Li, J., Beghein, C., Davis, P., Wieczorek, M. A., Mclennan, S. M., Kim, D., ... & Banerdt, W. B. (2022a). Crustal Structure Constraints from the Detection of the SsPp Phase on Mars. *Earth and Space Science*, e2022EA002416.

Li, J., Beghein, C., Wookey, J., Davis, P., Lognonné, P., Schimmel, M., Stutzmann, E., Golombek, M., Montagner, J.-P., and Banerdt, W. (2022b), Evidence for Crustal Seismic Anisotropy at the InSight Lander Site, *Earth and Planetary Science Letters*., 593, 117654, doi: 10.1016/j.epsl.2022.117654

Li., J., Beghein, C., Lognonné, P., McLennan, S., Wieczorek, M.A., Panning, M., Knapmeyer-Endrun, B., Davis, P., and Banerdt, W. (2022c), Different Martian Crustal Seismic Velocities across the Dichotomy Boundary from Multi-Orbiting Surface Waves, *Geophysical Research Letters*, 50, 1, doi:10.1029/2022GL101243

Li, J., Beghein, C., McLennan, S.M., Lognonné, P., Horleston, A.C., Charalambous, C., Huang, Q., Zenhäusern, G., Bozdag, E., Pike, T. W., Golombek M., Lekić, V., Lognonné, P., & Banerdt, W. (2022d), Second Seismic Anchor Point of the Martian Crustal Structure Away From the InSight Landing Site, *Nature Communications*, 13, 1, doi:10.1038/s41467-022-35662-y

Lognonné, P., Banerdt, W. B., Giardini, D., Pike, W. T., Christensen, U., Laudet, P., ... & Wookey, J. (2019). SEIS: Insight's seismic experiment for internal structure of Mars. *Space Science Reviews*, *215*, 1-170.

Lognonné, P., Banerdt, W. B., Pike, W. T., Giardini, D., Christensen, U., Garcia, R. F., ... & Zweifel, P. (2020). Constraints on the shallow elastic and anelastic structure of Mars from InSight seismic data. *Nature Geoscience*, 13(3), 213-220.

Menina, S., Margerin, L., Kawamura, T., Lognonné, P., Marti, J., Drilleau, M., ... & Banerdt, W. B. (2021). Energy envelope and attenuation characteristics of high-frequency (HF) and very-high-frequency (VF) Martian events. *Bulletin of the Seismological Society of America*, 111(6), 3016-3034.

Nissen-Meyer, T., van Driel, M., Stähler, S.C., Hosseini, K., Hempel, S., Auer, L., Colombi, A. and Fournier, A., 2014. AxiSEM: broadband 3-D seismic wavefields in axisymmetric media. *Solid Earth*, 5(1), pp.425-445.

Oberst, J. (1987). Unusually high stress drops associated with shallow moonquakes. *Journal of Geophysical Research: Solid Earth*, 92(B2), 1397-1405.

Posiolova, L. V., Lognonné, P., Banerdt, W. B., Clinton, J., Collins, G. S., Kawamura, T., ... & Zenhäusern, G. (2022). Largest recent impact craters on Mars: Orbital imaging and surface seismic co-investigation. *Science*, 378(6618), 412-417.

Sita, M., & van der Lee, S. (2022). Potential volcano-tectonic origins and faulting mechanisms of three low-frequency Marsquakes detected by a single InSight seismometer. *Journal of Geophysical Research: Planets*, e2022JE007309.

Solomon, S.C., Anderson, D.L., Banerdt, W.B., Butler, R.G., Davis, P.M., Duennebier, F.K., Nakamura, Y., Okal, E.A. and Phillips, R.J., 1991. Scientific rationale and requirements for a global seismic network on Mars. LPI Tech. Rept. 91-02. Lunar and Planetary Inst., Houston, TX.

Stähler, S.C., Mittelholz, A., Perrin, C., Kawamura, T., Kim, D., Knapmeyer, M., Zenhäusern, G., Clinton, J., Giardini, D., Lognonné, P. and Banerdt, W.B., 2022. Tectonics of Cerberus Fossae unveiled by marsquakes. *Nature Astronomy*, **6**, 1376–1386.

Stähler, S. C., Khan, A., Banerdt, W. B., Lognonné, P., Giardini, D., Ceylan, S., ... & Smrekar, S. E. (2021). Seismic detection of the martian core. *Science*, 373(6553), 443-448.

Tsai, Y. B., & Aki, K. (1970). Precise focal depth determination from amplitude spectra of surface waves. *Journal of Geophysical Research*, 75(29), 5729-5744.

van Driel, M., Krischer, L., Stähler, S. C., Hosseini, K., & Nissen-Meyer, T. (2015). Instaseis: Instant global seismograms based on a broadband waveform database. *Solid Earth*, 6(2), 701-717.

van Driel, M., Ceylan, S., Clinton, J. F., Giardini, D., Horleston, A., Margerin, L., ... & Banerdt, W. B. (2021). High-frequency seismic events on Mars observed by InSight. *Journal of Geophysical Research: Planets*, 126(2), e2020JE006670.